Journal of
Materials Chemistry A

ROYAL SOCIETY
OF CHEMISTRY

COMMUNICATION

View Article Online
View Journal | View Issue

Check for updates

Cite this: *J. Mater. Chem. A*, 2020, **8**, 5476

Received 17th December 2019
Accepted 16th February 2020

DOI: 10.1039/c9ta13785h

rsc.li/materials-a

A perovskite solar cell textile that works at −40 to 160 °C†

Limin Xu,[a] Xuemei Fu,[a] Fei Liu,[b] Xiang Shi,[a] Xufeng Zhou,[a] Meng Liao,[a]
Chuanrui Chen,[a] Fan Xu,[b] Bingjie Wang,[a] Bo Zhang[a] and Huisheng Peng *[a]

Environmental adaptability is an important factor in the practical application of flexible solar cells. This is particularly important in fiber-based solar cell textiles that are recently attracting increasing interest to solve application problems in a variety of emerging important fields such as in wearable and portable electronics. However, the difficult preparation of a compact active thin layer on a curved fiber surface and the interface instability under varying temperatures have largely limited the development of solar cell textiles. Here, we have made novel perovskite solar cell textiles by depositing a thin and continuous perovskite layer on aligned titanium dioxide nanotubes of fiber electrodes, and the aligned titanium dioxide nanotubes also functioned as an effective stress buffer layer for high interface stability. The power conversion efficiencies remained unchanged during storing at −20 or 100 °C for 240 h, and they could also be well maintained by 90% at a working temperature range of −40 to 160 °C.

Wearable and portable electronics that assist humankind in efficiently performing tasks are promising for various emerging important fields including wild expedition, polar research and space exploration. To this end, corresponding power supply systems are also highly required that have advantages of being lightweight and having flexibility, in order to satisfy the above applications. Fiber-based solar cell textiles have been thus explored to provide a general and effective solution as they are lightweight, flexible and breathable.[1–8] It was found that the solar cell textiles should be able to survive at a broad and fluctuating temperature range from seasonal variations to extreme temperature conditions, *i.e.* the average temperature of the South Pole is about −40 °C during the polar day and the highest temperature can be up to 127 °C on the moon in the daytime. However, the solar cell textiles that are currently available may work typically at room temperature, but they fail at relatively lower or higher temperatures. Dye-sensitized solar cell textiles suffer from electrolyte evaporation,[9–11] while polymer[12] and hybrid perovskite solar cell[13–16] textiles deteriorate at high temperatures.

Inorganic perovskite materials, such as $CsPbBr_3$, represent a promising light harvester material due to their high carrier mobility and long-term stability under cooling and heating.[17–21] However, it is not possible to deposit the $CsPbBr_3$ material to form a uniform layer on the curved surface of a fiber substrate.[22] It is even more difficult to maintain a stable $CsPbBr_3$ layer at varying temperatures. The thermal expansion coefficient of $CsPbBr_3$ (1.2×10^{-4} K^{-1}) is two orders of magnitude higher than those of the commonly used substrates such as fluorine-doped tin oxide (3.5×10^{-6} K^{-1}) and titanium (Ti) (8.5×10^{-6} K^{-1}).[21,23,24] The mismatch of the thermal expansion coefficient between the perovskite layer and the substrate leads to structural instability of the solar cell textile or even accelerates the degradation of the perovskite layer under stress at varying temperatures,[25,26] resulting in degraded performance or even failure of the device against temperature variation.

Herein, we have developed a new family of fiber-based perovskite solar cell textiles with a continuous and stable perovskite layer around the fiber electrodes at varying working temperatures. Aligned TiO_2 nanotubes on the fiber substrate were first synthesized on the surface of a Ti wire, and were found to effectively function as both a thermal stress buffer layer and as an electron transport layer. A continuous and robust $CsPbBr_3$ layer with grain sizes of ∼400 nm was achieved on the curved surface of the fiber substrate by a multiple-sintering method assisted by gap-filling of the $CsPbBr_3$ quantum dots (QDs). The solar cell textile effectively worked in the temperature range of −40 to 160 °C.

Perovskite materials could be easily coated onto film electrodes to form continuous active layers, to make planar perovskite solar cells through a typical two-step sequential deposition technique using spin coating.[27–32] However, it was difficult to

---

[a] State Key Laboratory of Molecular Engineering of Polymers, Department of Macromolecular Science, Laboratory of Advanced Materials, Fudan University, Shanghai 200438, China. E-mail: penghs@fudan.edu.cn

[b] Institute of Mechanics and Computational Engineering, Department of Aeronautics and Astronautics, Fudan University, Shanghai 200433, China

† Electronic supplementary information (ESI) available. See DOI: 10.1039/c9ta13785h

replicate the above fabrication process for fiber-shaped or textile-like solar cells due to the curved surface of the fiber substrate. Dip coating was thus adapted for the fiber electrodes. When this well-established sequential deposition[18] process with dip coating was used to prepare the fiber-shaped devices, the resulting $CsPbBr_3$ perovskite layer showed poor coverage with a lot of pinholes (Fig. S1a and b†). Repeating the deposition process led to obvious aggregations of $CsPbBr_3$ particles, without the formation of the expected uniform and continuous layer (Fig. S1c†). No fiber-shaped solar cell that worked effectively could be fabricated through this method, and the PCE of the obtained device was only 0.0005% (Fig. S2†).

Therefore, a multiple sintering method was discovered to gain full-coverage and obtain a uniform perovskite layer with large sized crystals on the curved surface of the fiber substrate. The specific fabrication process is schematically shown in Fig. 1a. Briefly, $CsPbBr_3$ QDs were first synthesized by a room-temperature triple-ligands method (Fig. S3 and S4†).[33] Aligned TiO_2 nanotubes were grown on the surface of a Ti wire through an anodization process. The modified Ti wire was dipped into the $CsPbBr_3$ QDs solution to form a thin layer on the curved surface (Fig. 1b). Then, a sintering procedure was performed to avoid the re-soluble problem of QDs in the repeated dip-coating process. Note that sintering also resulted in the transformation of the $CsPbBr_3$ QDs into bulk $CsPbBr_3$ (Fig. 1c). The $CsPbBr_3$ film annealed at both 250 °C and 300 °C, and exhibited an absorption peak at 515 nm, while $CsPbBr_3$ NCs showed an absorption peak at 505 nm (Fig. S5†). This shift in absorption is consistent with the formation of bulk $CsPbBr_3$.[34] However, didodecyldimethylammonium bromide (DDAB), the organic ligand that was used in this process, still existed when annealing occurred at 250 °C but was almost entirely removed at 300 °C (Fig. S6†). Thus, the annealing temperature of 300 °C was used here to eliminate the unstable organic component. Then, the modified Ti wire was dipped again into the $CsPbBr_3$ QDs solution to fill the gaps among the $CsPbBr_3$ crystals with $CsPbBr_3$ QDs (Fig. 1d), which benefited from the small sizes of the $CsPbBr_3$ QDs (Fig. S7†). Sintering treatment was applied afterwards to transform the newly added QDs into large crystals. This process was repeated for several cycles until a compact and uniform photoactive layer (Fig. 1e) with grain sizes of ~400 nm (Fig. S8†) was obtained. Finally, the whole TiO_2 modified Ti wire was evenly covered with $CsPbBr_3$ crystals (Fig. 1f–h).

Fiber-shaped $CsPbBr_3$ perovskite solar cells were fabricated with a coaxial architecture (Fig. 2a), consisting of a TiO_2 nanotube modified Ti wire serving as a working electrode (Fig. S9a

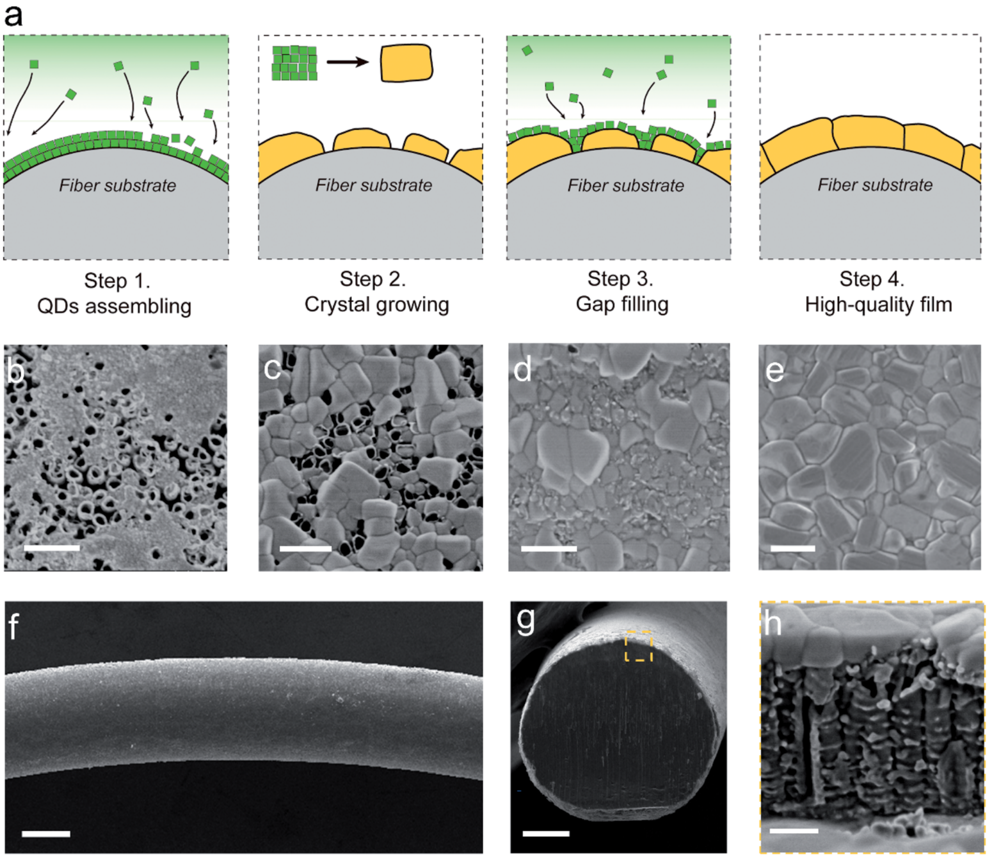

Fig. 1 A compact $CsPbBr_3$ film formed on the curved fiber substrate. (a) Schematic illustration of the fabrication process of the compact $CsPbBr_3$ layer. (b–e) SEM images of the TiO_2 nanotube-modified Ti wire coated with quantum dots (b), after annealing (c), after quantum dots filling up the gaps between large-grain $CsPbBr_3$ (d), and of the compact $CsPbBr_3$ layer (e). Scale bar is at 400 nm. (f–h) SEM images of the Ti wire coated with a $CsPbBr_3$ layer (f), the cross section of the modified Ti wire (g), and of the interface between the $CsPbBr_3$ layer and the TiO_2 nanotubes (h). Scale bars are at 100 μm in (f), 50 μm in (g) and 200 nm in (h).

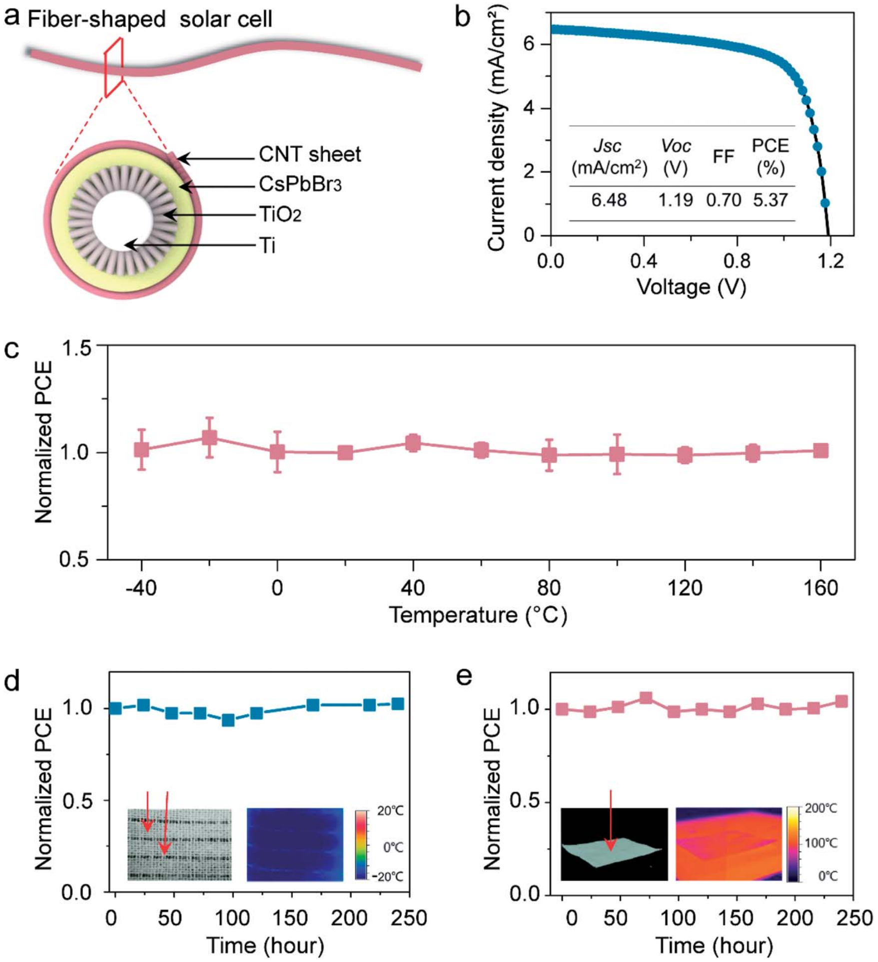

Fig. 2 $CsPbBr_3$ perovskite solar cell textiles working at room, low and high temperatures. (a) Schematic illustration of the fiber-shaped solar cell. (b) Typical *J*–*V* curves of the fiber-shaped solar cell with a power conversion efficiency of 5.37%. The inserted table shows the corresponding photovoltaic parameters. (c) Normalized PCE values as a function of the working temperature. (d and e) Normalized PCE as a function of the storing time at −20 °C and at 100 °C, respectively, without encapsulation.

and b†), a $CsPbBr_3$ perovskite layer, and an aligned carbon nanotube (CNT) sheet working as another electrode (Fig. S9c†). Here, the aligned TiO_2 nanotubes were grown in the radial direction of the Ti wire through electrochemical anodic oxidation. The *in situ* growth guaranteed the integration of Ti and TiO_2, which benefited the flexibility and mechanical stability of the resulting device. The porous structure of the TiO_2 nanotube acted as a stress buffer layer, and the aligned structure of the TiO_2 nanotube ensured the direct transport of electrons. It is worth noting that the outermost layer of the CNT sheet served as a bifunctional layer for hole extraction and collection. In addition, the CNT sheet had an appropriate work function (−4.8 eV), high transparency and high thermal stability. The rational design for the above combined properties was critical for the high thermal stability of the assembled device.

The photovoltaic performances depended on the film thickness of the $CsPbBr_3$ layer, and this could be controlled by varying the dip-coating cycle number (Table S1, Fig. S10†). The PCE increased when the dip-coating cycle number increased from 60 to 120, due to the improved coverage and film thickness of the photoactive $CsPbBr_3$ layer (Fig. S11†). However, the thicker film became unfavorable for carrier separation at a dip-coating cycle number of 150, and exhibited a clear decrease of PCE. The maximal PCE reached 5.37% (Fig. 2b). Moreover, the device exhibited a minor hysteresis between the forward and reverse scanning modes (Fig. S12†). Note that all fabrication processes were performed in an ambient environment without deliberate control over the environmental humidity and temperature.

In order to demonstrate the stability against the varying temperatures, the photovoltaic devices without encapsulation were stored at different temperatures for 15 min before testing. At a wide temperature range from −40 to 160 °C, the PCEs were well maintained by 90% (Fig. 2c), indicating that the fiber shaped $CsPbBr_3$ perovskite solar cells operated stably within this temperature range. Meanwhile, the long-term stability at low or high temperatures was another important factor in assessing its practicability. Here, they were stored at −20 °C and 100 °C in order to investigate the long-term stability in harsh temperature conditions. The PCEs were also maintained by over

90% for 240 h in both conditions (Fig. 2d and e). In addition, the photocurrent density and PCE as a function of time were measured at MPP with devices placed at −20 and 100 °C, and these remained stable for a 100 s scan (Fig. S13 and S14†).

For applications with varying temperatures, the structural instability mainly accounts for the failure of the device, which originates from the mismatch of the thermal expansion coefficients between the perovskite layer and the substrate. More specifically, the thermal expansion coefficient of $CsPbBr_3$ (1.2×10^{-4} K^{-1}) is two orders of magnitude higher than that of the TiO_2 (8.2×10^{-6} K^{-1}) or Ti (8.5×10^{-6} K^{-1}) substrate. This mismatch will cause a thermal stress on the near-interface regions at varying temperatures. Finite element analysis relative to the decreasing temperature was conducted to visualize this process. As is schematically shown in Fig. 3a, for a photovoltaic device with a dense TiO_2 layer as the electron transport layer, thermal stress was concentrated around the interface between the perovskite layer and the dense TiO_2 layer. Here, aligned and porous TiO_2 nanotubes have been designed to relieve the mismatch of the thermal stress. A porous structure poses less restriction to the deformation of $CsPbBr_3$ during temperature variation, and thus can effectively relieve the residual interfacial thermal stress in the $CsPbBr_3$ layer. As expected, the result of the simulation showed that there was less concentration of thermally induced stress mismatch at the interface of $CsPbBr_3$ and the porous TiO_2 nanotube layer than between $CsPbBr_3$ and the dense TiO_2 layer (right panels of Fig. 3a).

To further confirm the positive effect of TiO_2 nanotubes on the structural stability of the device, out-of-plane X-ray diffraction (XRD) was conducted to assess the stress of $CsPbBr_3$ on different structures of TiO_2. The compression stress in the

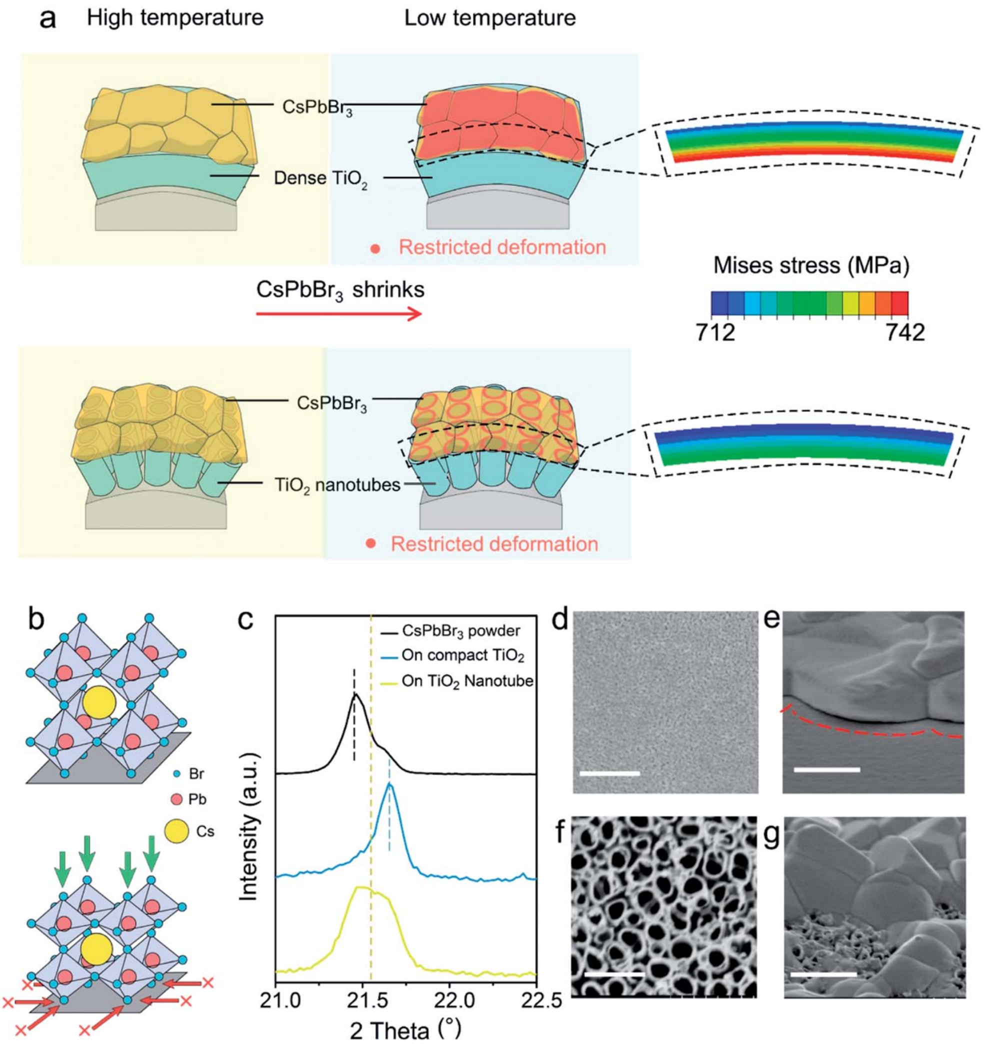

Fig. 3 Mechanism of the compact $CsPbBr_3$ film stabilized on the curved fiber substrate under varying temperatures. (a) Schematic illustration of the thermal stress release by the aligned TiO_2 nanotubes with finite element simulation of the $CsPbBr_3$ layer. (b) Schematic diagram of the strain formation process. The annealed perovskite film contracts perpendicularly with the substrate adhesion. (c) XRD patterns of the $CsPbBr_3$ powder (black line), the annealed $CsPbBr_3$ layer on the compact TiO_2 substrate (blue line) and of the annealed $CsPbBr_3$ layer on the aligned TiO_2 nanotube substrate (yellow line). (d) SEM image of the compact TiO_2 layer. Scale bar is at 300 nm. (f) SEM image of the aligned TiO_2 nanotube layer. Scale bar is at 300 nm. (e and g) Interface between the $CsPbBr_3$ layer and the compact TiO_2 substrate, and between the $CsPbBr_3$ layer and the TiO_2 nanotube substrate after cooling from 300 to 20 °C, respectively. Scale bar is at 300 nm.

$CsPbBr_3$ film in the vertical direction leads to smaller plane spacing (Fig. 3b), and this corresponds to a shift in the diffraction peaks to higher diffraction angles in the out-of-plane XRD patterns.[35] The tested samples were all annealed at 300 °C and were cooled to room temperature before the tests. In addition, $CsPbBr_3$ powder was used as a stress-free sample. As illustrated in Fig. 3c, both $CsPbBr_3$ films with TiO_2 nanotubes and a compact TiO_2 layer displayed higher peak shifts relative to the $CsPbBr_3$ powder. However, the former showed a much smaller shift to high diffraction angles by 0.08°, while the shift was 0.18° for the compact TiO_2 layer, and this smaller shift of the $CsPbBr_3$ film on the TiO_2 nanotubes implies less compression stress.

Furthermore, the samples with the TiO_2 layer partially covered by $CsPbBr_3$ were specially prepared for better observation of the interface relative to thermal expansion mismatch. The defects induced by residual thermal stress can be directly observed on the interface between the $CsPbBr_3$ layer and the compact TiO_2 layer, where gaps with sizes of ~10 nm emerged (Fig. 3d and e). On the contrary, the $CsPbBr_3$ layer was bonded closely with the top of the TiO_2 nanotubes (Fig. 3f and g). Hence, fiber-shaped solar cells based on a TiO_2 nanotube layer showed significantly enhanced stability (Fig. 2c), while their counterparts with only a compact TiO_2 layer showed a retention of 58% of their original value when the temperature increased from 20 to 160 °C (Fig. S15†).

These robust fiber-shaped solar cells were further woven into textiles for wearable applications, especially under extreme environments (Fig. 4a). The solar cell textile showed high flexibility following the deformation process. After bending at 45° for 5000 cycles, the solar cell textile maintained over 90% of its original PCE (Fig. 4b). The output voltage and current of the textile could also be designed to satisfy different applications. The short-circuit current (I_{sc}) of the textile with fiber-shaped devices connected in parallel increased linearly with the device number while the open-circuit voltage (V_{oc}) remained almost unchanged (Fig. 4c). For instance, a solar cell textile with an I_{sc} value of 0.45 mA and a V_{oc} value of 1.22 V was obtained by integrating five devices with lengths of ~2.5 cm in parallel. For the five devices connected in series, an I_{sc} value of 0.09 mA and a V_{oc} value of 6.22 V could be achieved (Fig. 4d). The resulting solar cell textile was easily adapted to human skin to power an electronic watch in an ambient environment under solar irradiation (Fig. 4e). More importantly, it could also successfully work under extreme conditions. For instance, it could even work whilst being frozen in ice with a waterproof layer as encapsulation, and the solar cell textile worked without disturbance (Fig. 4f). In an extremely hot environment, the solar cell textile still effectively powered an electronic clock when it was placed on glowing charcoal (Fig. 4g).

In conclusion, a new family of inorganic perovskite solar cell fibers and textiles has been fabricated *via* a multiple-sintering method. The compact $CsPbBr_3$ perovskite layer supported by aligned TiO_2 nanotubes that functioned as a stress buffer and as an electron transport layer on the curved surface of the fiber substrate meant that the solar cells were able to work at −40 to 160 °C with both high long-term stability and a high PCE. This work opens up a new avenue towards the design of temperature-resistant wearable solar cells, especially in applications at extreme temperatures.

Experimental section

Materials

All purchased materials were used as received without further purification unless mentioned. Ti wires (diameter of 250 μm, 99.9%) were obtained from Alfa Aesar. Cesium carbonate (Cs_2CO_3), lead bromide ($PbBr_2$), ammonium fluoride (NH_4F), tetraoctylammonium bromide (TOAB), octanoic acid (OTAc), titanium diisopropoxide bis(acetylacetonate) solution and didodecyldimethylammonium bromide (DDAB) were ordered from Sigma-Aldrich. Perchloric acid ($HClO_4$), ethylene glycol monobutylether, methanol, toluene and hexane were purchased from Sinopharm Chemical Reagent Co., Ltd.

Preparation of the compact TiO_2 layer and the aligned TiO_2 nanotube layer

A Ti wire was polished *via* an electrolytic polishing method at a voltage of 35 V for 15 s followed by polishing at 20 V for 20 s, to yield a clear and smooth surface. The polishing electrolyte contained 5 wt% $HClO_4$, 53 wt% ethylene glycol monobutylether and 42 wt% methanol. Afterwards, the Ti wire was washed with deionized water under sonication for 20 min and then dried at 80 °C in an oven. For preparation of the compact TiO_2 layer, a polished Ti wire was dip-coated in a 75 wt% titanium diisopropoxide bis(acetylacetonate) solution and dried at 125 °C. The coated Ti wire was further annealed at 400 °C for 30 min in air. For the aligned TiO_2 nanotube layer, the polished Ti wire was anodized at 20 V for 7 min in an electrolyte containing 0.27 M NH_4F in a solvent mixture of water and glycerol (volume ratio, 1/1). After anodizing and washing with deionized water, the resulting Ti wire was annealed at 500 °C for 60 min.

Synthesis of $CsPbBr_3$ quantum dots

$CsPbBr_3$ quantum dots were synthesized by a room-temperature triple-ligand method. First, the cesium precursor was prepared by dissolving 0.0543 g of Cs_2CO_3 into 10 mL of OTAc. The $PbBr_2$ precursor was prepared by mixing 0.0367 g of $PbBr_2$ and 0.1092 g of TOAB in 6 mL of toluene. Subsequently, 0.67 mL of the cesium precursor solution was added to the $PbBr_2$ precursor solution under magnetic stirring in the open air. After reacting for 5 min, 2 mL of DDAB (10 mg mL^{-1} in toluene) was added to the mixture. The mixture was further stirred for 2 min before being washed by 20 mL ethyl acetate. Then the precipitate was collected after centrifugation (10 000 rpm, 5 min) and dissolved in 10 mL of toluene. 20 mL ethyl acetate was added again to resuspend the QDs. The final precipitate was re-dispersed in 5 mL of hexane for further use.

Fabrication of the fiber-shaped perovskite solar cell

For the multiple-sintering method, the TiO_2 modified Ti wire was dipped into the $CsPbBr_3$ quantum dot solution and annealed at 300 °C to remove the organic ligands of the quantum dots. The

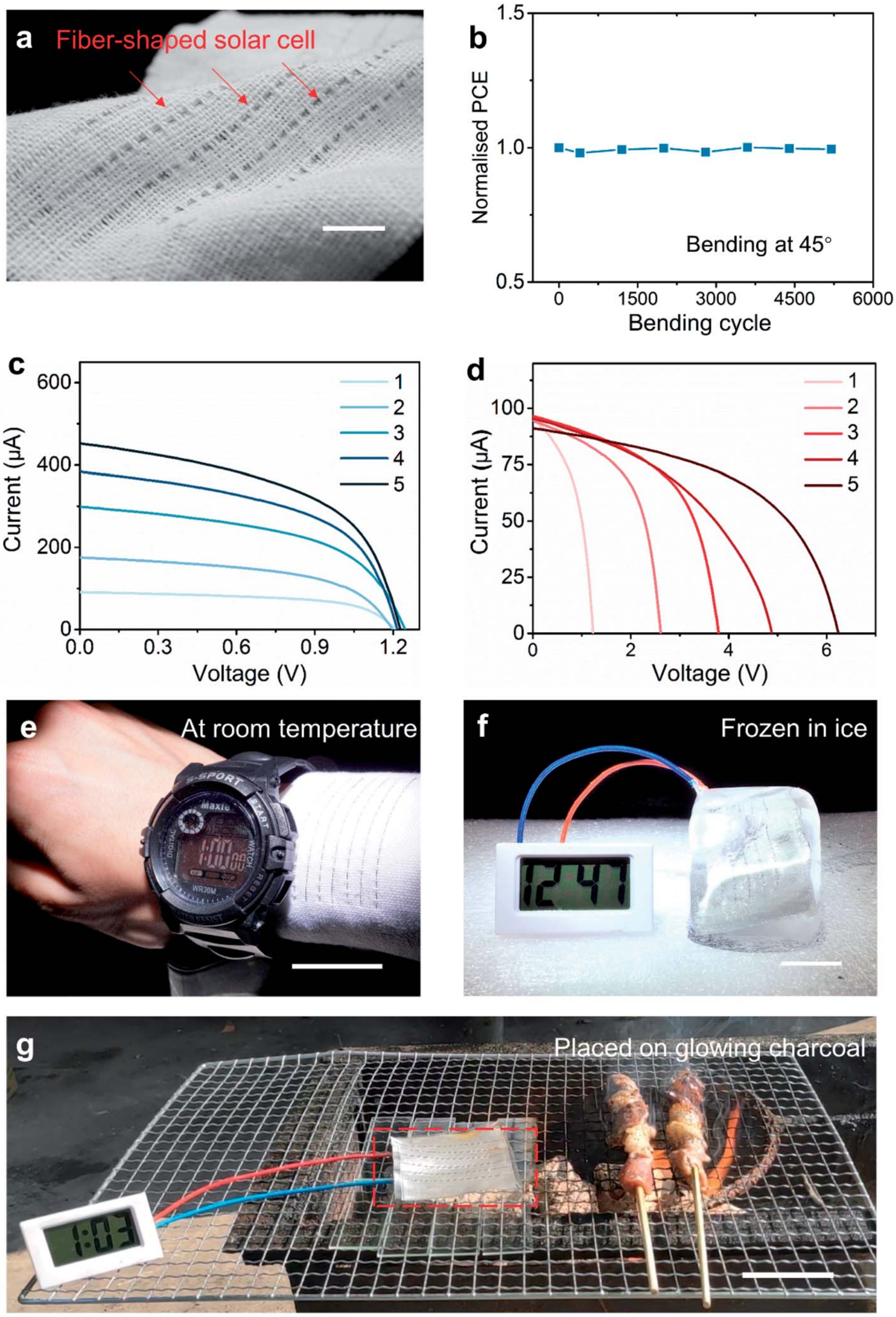

Fig. 4 Application demonstration of the solar cell textiles in harsh conditions. (a) Photograph of a perovskite solar cell textile. Scale bar is at 1 cm. (b) Dependence of PCE on bending cycle with a bending angle of 45°. (c and d) *I*–*V* curves of the textiles with fiber-shaped perovskite solar cells connected in parallel and in series, respectively. (e) A solar cell textile at room temperature powering an electronic watch under solar irradiation. Scale bar is at 2 cm. (f) Demonstration of the solar cell textile frozen in ice powering the electronic clock under solar irradiation. Scale bar is at 2 cm. (g) Demonstration of the solar cell textile placed on glowing charcoal powering the electronic clock under outdoor sunlight. Scale bar is at 4 cm.

thickness of the $CsPbBr_3$ perovskite layer could be controlled by repeating this coating process. After this, an aligned CNT sheet was further wrapped around the $Ti/TiO_2/CsPbBr_3$ wire. Then a droplet of hexane was finally dropped onto the CNT sheet, and the device was annealed at 80 °C to enhance the contact between the CNT sheet and the $CsPbBr_3$ crystal. For the two-step sequential deposition technique,[18] 1 M of $PbBr_2$ in DMF was stirred at 70 °C for 20 min and filtered using a 0.2 μm pore size PTFE filter. The preheated (70 °C) TiO_2 modified Ti wire was then dipped into this solution and dried on a hot plate at 75 °C for 20 min. After drying, the TiO_2 modified Ti wire was dipped in a heated (50 °C) solution of 15 mg mL^{-1} CsBr in methanol for 10 min and annealed for 10 min at 250 °C. This process was repeated to increase the film thickness of $CsPbBr_3$.

Finite element analysis

A finite element method was used to simulate the thermally induced stress field in $CsPbBr_3$ and in the dense TiO_2 layer/porous TiO_2 nanotube layers, using the commercial software Abaqus. Considering the negligible deformation of the Ti wire with a radius of 100 μm during temperature variation, we only modeled $CsPbBr_3$ and TiO_2 layers under the plane strain condition, and the interface between the TiO_2 layer and the Ti wire can be viewed as a fixed boundary condition. The thickness of the $CsPbBr_3$ and TiO_2 layers were 300 nm and 600 nm, respectively. In the simulations, the elastic modulus values of the $CsPbBr_3$, dense TiO_2 and porous TiO_2 nanotube layers were 16, 230 and 20 GPa, and the Poisson's ratios of these materials were set to 0.28. The expansion coefficients were $1.2 \times 10^{-4}\ K^{-1}$ for $CsPbBr_3$ and $8.2 \times 10^{-6}\ K^{-1}$ for dense/aligned TiO_2. When the temperature was dropped from 300 °C to 25 °C, the heat transfer problem was linear because the properties of the material are independent of temperature. Then, the simulations were performed using steady-state analysis to acquire a thermally induced stress field. Convergent solutions were obtained using 133974 CPE4 elements (4-node bilinear plane strain quadrilateral). The expansion coefficients of the dense TiO_2 and porous TiO_2 nanotube layers are identical, which results in the same thermal mismatch strains at the same temperature variation. Therefore, compared with the dense TiO_2 layer, the porous TiO_2 nanotube layer with a smaller elastic modulus leads to a smaller mismatch in thermal stress at the interface.

Characterization

J–V curves of the photovoltaic textiles were recorded using a Keithley 2400 Source Meter under illumination (100 mW cm^{-2}) of a simulated AM1.5 solar light from a solar simulator (Oriel-Sol3A 94023A equipped with a 450 W Xe lamp and an AM1.5 filter). The morphology and structure were characterized by field-emission SEM (Ultra 55, Zeiss). The XRD experiments were performed with a Bruker D8 Advance diffractometer. The morphology of the $CsPbBr_3$ QDs was characterized by transmission electron microscopy (JEM-1400plus). The morphology of $CsPbBr_3$ on the modified-Ti wire using the two-step solution seven times was obtained by light microscopy (OLYMPUS BX51).

Conflicts of interest

There are no conflicts to declare.

Acknowledgements

This work was supported by MOST (2016YFA0203302), NSFC (21634003, 51573027, 21604012, 11872150, 11602058, and 21875042), STCSM (16JC1400702, 19QA1400500, 18QA1400700, and 18QA1400800), SHMEC (2017-01-07-00-07-E00062), SEDF (16CG01), and by the Yanchang Petroleum Group.

References

1 Z. Chai, N. Zhang, P. Sun, Y. Huang, C. Zhao, H. J. Fan, X. Fan and W. Mai, *ACS Nano*, 2016, **10**, 9201–9207.
2 X. Fu, H. Sun, S. Xie, J. Zhang, Z. Pan, M. Liao, L. Xu, Z. Li, B. Wang, X. Sun and H. Peng, *J. Mater. Chem. A*, 2018, **6**, 45–51.
3 P. Liu, Z. Gao, L. Xu, X. Shi, X. Fu, K. Li, B. Zhang, X. Sun and H. Peng, *J. Mater. Chem. A*, 2018, **6**, 19947–19953.
4 L. Qiu, S. He, J. Yang, F. Jin, J. Deng, H. Sun, X. Cheng, G. Guan, X. Sun, H. Zhao and H. Peng, *J. Mater. Chem. A*, 2016, **4**, 10105–10109.
5 N. Zhang, J. Chen, Y. Huang, W. Guo, J. Yang, J. Du, X. Fan and C. Tao, *Adv. Mater.*, 2016, **28**, 263–269.
6 Y. Hong, X. Cheng, G. Liu, D. Hong, S. He, B. Wang, X. Sun and H. Peng, *Chin. J. Polym. Sci.*, 2019, **37**, 737–743.
7 X. Wu and H. Peng, *Sci. Bull.*, 2019, **64**, 634–640.
8 X. Fu, Z. Zhuo, L. Xu, M. Liao, H. Sun, S. Xie, X. Sun, B. Wang and H. Peng, *Sci. China Mater.*, 2019, **62**, 955–964.
9 H. Li, J. Guo, H. Sun, X. Fang, D. Wang and H. Peng, *ChemNanoMat*, 2015, **1**, 399–402.
10 H. Sun, H. Li, X. You, Z. Yang, J. Deng, L. Qiu and H. Peng, *J. Mater. Chem. A*, 2014, **2**, 345–349.
11 D. Zhang, H. Yin, Z. Li, Y. Zhou, T. Yu, J. Liu and Z. Zou, *RSC Adv.*, 2015, **5**, 65005–65009.
12 J. U. Lee, J. W. Jung, J. W. Jo and W. H. Jo, *J. Mater. Chem.*, 2012, **22**, 24265–24283.
13 C. C. Boyd, R. Cheacharoen, T. Leijtens and M. D. McGehee, *Chem. Rev.*, 2019, **119**, 3418–3451.
14 B. Conings, J. Drijkoningen, N. Gauquelin, A. Babayigit, J. D'Haen, L. D'Olieslaeger, A. Ethirajan, J. Verbeeck, J. Manca, E. Mosconi, F. D. Angelis and H.-G. Boyen, *Adv. Energy Mater.*, 2015, **5**, 1500477.
15 A. Dualeh, P. Gao, S. I. Seok, M. K. Nazeeruddin and M. Grätzel, *Chem. Mater.*, 2014, **26**, 6160–6164.
16 T. Supasai, N. Rujisamphan, K. Ullrich, A. Chemseddine and T. Dittrich, *Appl. Phys. Lett.*, 2013, **103**, 183906.
17 J. Duan, T. Hu, Y. Zhao, B. He and Q. Tang, *Angew. Chem., Int. Ed.*, 2018, **57**, 5746–5749.
18 M. Kulbak, D. Cahen and G. Hodes, *J. Phys. Chem. Lett.*, 2015, **6**, 2452–2456.
19 M. Kulbak, S. Gupta, N. Kedem, I. Levine, T. Bendikov, G. Hodes and D. Cahen, *J. Phys. Chem. Lett.*, 2016, **7**, 167–172.
20 I. Poli, J. Baker, J. McGettrick, F. De Rossi, S. Eslava, T. Watson and P. J. Cameron, *J. Mater. Chem. A*, 2018, **6**, 18677–18686.
21 C. C. Stoumpos, C. D. Malliakas, J. A. Peters, Z. Liu, M. Sebastian, J. Im, T. C. Chasapis, A. C. Wibowo, D. Y. Chung, A. J. Freeman, B. W. Wessels and M. G. Kanatzidis, *Cryst. Growth Des.*, 2013, **13**, 2722–2727.
22 L. Qiu, S. He, J. Yang, J. Deng and H. Peng, *Small*, 2016, **12**, 2419–2424.
23 L. Fu, P. Lever, H. H. Tan, C. Jagadish, P. Reece and M. Gal, *Appl. Phys. Lett.*, 2003, **82**, 2613–2615.

24 T. J. Jacobsson, L. J. Schwan, M. Ottosson, A. Hagfeldt and T. Edvinsson, *Inorg. Chem.*, 2015, **54**, 10678–10685.

25 J. Deng, L. Qiu, X. Lu, Z. Yang, G. Guan, Z. Zhang and H. Peng, *J. Mater. Chem. A*, 2015, **3**, 21070–21076.

26 N. Rolston, K. A. Bush, A. D. Printz, A. Gold-Parker, Y. Ding, M. F. Toney, M. D. McGehee and R. H. Dauskardt, *Adv. Energy Mater.*, 2018, **8**, 1802139.

27 X. Chang, W. Li, L. Zhu, H. Liu, H. Geng, S. Xiang, J. Liu and H. Chen, *ACS Appl. Mater. Interfaces*, 2016, **8**, 33649–33655.

28 J. Ding, Y. Zhao, J. Duan, B. He and Q. Tang, *ChemSusChem*, 2018, **11**, 1432–1437.

29 J. Duan, Y. Zhao, B. He and Q. Tang, *Angew. Chem., Int. Ed.*, 2018, **57**, 3787–3791.

30 J. Duan, Y. Zhao, X. Yang, Y. Wang, B. He and Q. Tang, *Adv. Energy Mater.*, 2018, **8**, 1802346.

31 J. Liang, C. Wang, Y. Wang, Z. Xu, Z. Lu, Y. Ma, H. Zhu, Y. Hu, C. Xiao, X. Yi, G. Zhu, H. Lv, L. Ma, T. Chen, Z. Tie, Z. Jin and J. Liu, *J. Am. Chem. Soc.*, 2016, **138**, 15829–15832.

32 H. Yuan, Y. Zhao, J. Duan, Y. Wang, X. Yang and Q. Tang, *J. Mater. Chem. A*, 2018, **6**, 24324–24329.

33 J. Song, J. Li, L. Xu, J. Li, F. Zhang, B. Han, Q. Shan and H. Zeng, *Adv. Mater.*, 2018, **30**, 1800764.

34 J. B. Hoffman, A. L. Schleper and P. V. Kamat, *J. Am. Chem. Soc.*, 2016, **138**, 8603–8611.

35 J. Zhao, Y. Deng, H. Wei, X. Zheng, Z. Yu, Y. Shao, J. E. Shield and J. Huang, *Sci. Adv.*, 2017, **3**, eaao516.